



Superoxide ($\cdot\text{O}_2^-$) radical species driven type II $\text{TiO}_2/\text{g-C}_3\text{N}_4$ heterojunction photocatalyst for RhB dye degradation

Smita M. Yadav¹, Mangesh A. Desai^{1,*}, and Shrikrishna D. Sartale^{1,*}

¹Thin Films and Nanomaterials Laboratory, Department of Physics, Savitribai Phule Pune University, Pune 411007, India

Received: 15 March 2023

Accepted: 20 July 2023

Published online:
10 August 2023

© The Author(s), under exclusive licence to Springer Science+Business Media, LLC, part of Springer Nature 2023

ABSTRACT

The photocatalysts possess prime importance from sustainable environment view point since they decompose detrimental substances. In this work, we report a type II heterojunction of titanium dioxide/graphitic carbon nitride ($\text{TiO}_2/\text{g-C}_3\text{N}_4$) photocatalysts for degradation of rhodamine B (RhB) dye under UV-Visible light irradiation. The pristine TiO_2 and $\text{g-C}_3\text{N}_4$ materials are prepared by hydrothermal and thermolysis methods, respectively. The heterojunction photocatalysts, i.e. $\text{TiO}_2/\text{g-C}_3\text{N}_4$ are synthesized with different weight% (wt%) loadings of TiO_2 over $\text{g-C}_3\text{N}_4$ by hydrothermal method. The physico-chemical properties of all photocatalysts are analysed by different characterization techniques. Compared with the pristine phase of TiO_2 and $\text{g-C}_3\text{N}_4$, the heterojunction photocatalysts showed improved efficiency due to effective charge transfer between TiO_2 with $\text{g-C}_3\text{N}_4$ and enhanced visible light harvesting. Owing to effective superlative light absorption and generation of the large number of electron-hole pairs, suppression of recombination centres, formation of active species (specially $\cdot\text{O}_2^-$), etc., 5 wt% loaded $\text{TiO}_2/\text{g-C}_3\text{N}_4$ photocatalyst demonstrated superior performance. Moreover, 5 wt% loaded $\text{TiO}_2/\text{g-C}_3\text{N}_4$ photocatalyst exhibited recyclability with high activity (92% after 4 cycles) and thus, we believe it possesses potential for use in industrial water treatment.

1 Introduction

Increasing industrialization brings out extensive environmental contamination caused by pollution in air, water, soil, etc. Amongst polluted water infiltrating from several textile, chemical and other

industries is severely affecting human beings, vegetation and aquatic animals from past many years. Hence, wastewater management is considered as the world wide prime task for the mankind. All over the world, around one million tons of coloured effluent are estimated to be released from the dye industries [1]. Decomposition of such pollutants into non-toxic

Address correspondence to E-mail: desaiever@gmail.com; sdsartale@physics.unipune.ac.in

by products is very essential via eco-friendly treatment.

Photocatalytic degradation of organic pollutant is a potential method and nowadays, it has received attractive attention due to its high efficiency, low toxicity, reliability and sustainability [2–5]. Therefore, the design and development of such semiconductor photocatalyst that can work efficiently under visible light are of utmost importance at present. In the hunt, a number of metal oxides [6], nitrides [7] and metal chalcogenides [8] have been reported as photocatalysts for the treatment of organic pollutants present in water [9, 10]. However, most of them are far from practical usage because of their impotency to catch visible light and less chemical and structural stability.

On the other hand, industrial water pollution created several ecological and biological problems. Modern wastewater purification approaches can give rise to sustainable environmental solutions. For instance, photocatalytic processes can be easily applied for industrial effluents treatment and wastewater can be reused.

Amongst different stable photocatalysts, TiO_2 is the predominant photocatalyst because of different advantages like non-toxicity, high chemical and structural stability and less expensive and is thus used for degradation of numerous pollutants. However, because of its high bandgap, its photocatalytic performance is dependent only on UV radiation and no absorption of visible light takes place leading to underrated photocatalytic activity [11, 12]. To encounter this problem, different strategies have been employed such as doping, formation of heterojunction, and decoration with noble and non-noble nanoparticles for improving the photocatalytic activity. Amongst above-said strategies, heterojunction formation with TiO_2 is most believed route in scientific community due to its efficacy for the spatial separation of $e^- - h^+$ [13, 14]. Moreover, depending on coupled material several types of TiO_2 heterojunction are preferred, such as type II heterojunction (may be p–n or n–n) [15], surface heterojunction, and direct Z-scheme heterojunction [16–18]. In recent years, due to non-toxic, layered structure, non-metal and inexpensive graphitic carbon nitride ($\text{g-C}_3\text{N}_4$) has emerged as a promising metal-free visible light photocatalyst for hydrogen production from water. This photocatalyst has many advantageous properties to form heterojunction with TiO_2 , such as appropriate bandgap, excellent chemical stability,

visible light absorption and high conductivity [19–22].

In order to form heterojunctions, several synthesis methods are being used. Amongst all, hydrothermal synthesis provides many advantages, such as relatively easy operating conditions, one-step synthesis, ability to produce various morphologies and crystal phases, eco-friendly nature, and mass productive. In hydrothermal synthesis method, the consistent morphology, phase and particle size of the nanomaterials can be achieved by keeping all the synthesis parameters constant.

Considering individual TiO_2 or $\text{g-C}_3\text{N}_4$ species, its heterojunction overcomes all difficulties faced by individual material. It improves the photocatalytic performance due to synergistic effects, such as enhanced light harvesting, improved photostability, and efficient photoexcited charge separation. In the present work, our attention is to synthesize efficient $\text{TiO}_2/\text{g-C}_3\text{N}_4$ heterojunction photocatalyst for rhodamine B (RhB) dye degradation. We have prepared pristine $\text{g-C}_3\text{N}_4$ by thermolysis method. In our work, controlled mass loading of TiO_2 over $\text{g-C}_3\text{N}_4$, i.e. $\text{TiO}_2/\text{g-C}_3\text{N}_4$ heterojunctions was possible with hydrothermal method. For the said purpose, various weight% (wt%) of TiO_2 were taken with respect to $\text{g-C}_3\text{N}_4$, i.e. 2.5, 5 and 7.5 wt% $\text{TiO}_2/\text{g-C}_3\text{N}_4$ and named as 2.5TG, 5TG, and 7.5TG, respectively. These prepared samples were used to check further for finding out better photocatalyst for RhB dye degradation. The main purpose is to find out and understand optimum loading of TiO_2 for better photocatalytic performance towards RhB dye degradation.

2 Materials and methods

2.1 Materials

All chemicals were of analytical grade and used without further purification. Titanium tetraisopropoxide (TTIP) was procured from Spectrochem, India. Iso-propyl alcohol (IPA) was obtained from Thomas Baker, India. Melamine, RhB, dimethyl sulfoxide (DMSO), ascorbic acid (AA), sodium chloride, sodium hydroxide, hydrochloric acid and methanol were purchased from Sigma-Aldrich, India. Double distilled water (DDW) was used for all the experiments.

2.2 Synthesis of photocatalysts

The g-C₃N₄ be the host material prepared by commonly used conventional one-step thermolysis technique [23, 24]. In a typical process, a certain amount of melamine (4 g) was placed in a partially sealed alumina crucible with a quartz covering. It was directly heated in the tube furnace under ambient atmosphere at temperature 500 °C with heating rate ~ 3 °C/min for two hours. To have controlled evaporation, the alumina crucible was partially sealed. Afterwards, the powder was allowed to cool naturally inside the tube furnace itself. The obtained yellow fine powder was collected for further use.

In the heterojunction photocatalyst synthesis, TiO₂ was loaded on g-C₃N₄ using hydrothermal method. Two separate solutions were prepared. In the first beaker, an appropriate amount of g-C₃N₄ was added in the mixture of TTIP (precursor for TiO₂) and IPA (solvent). The mixture of IPA and DDW with fixed (1:1) volume ratio was taken in second beaker. Here, the concentration of TTIP decides amount of TiO₂ nanoparticles and the volume of water decides the size of nanoparticles [25]. Solution from the second beaker was added drop wise in the first beaker and kept under constant vigorous stirring for 2 h. The stirring time was kept constant for all experiments. Furthermore, the solution was transferred in Teflon-lined stainless steel autoclave and sealed it for heating in a hot air oven at 175 °C for 24 h. Afterwards, autoclave cooled naturally to room temperature (this process took 6 h). The mother liquor was separated and precipitate was collected. To remove out the impurities the precipitate washed several times using DDW and ethanol. This yield was then dried in hot air oven at 90 °C, till complete drying. The heterojunction photocatalysts such as, 2.5TG, 5TG, and 7.5TG were synthesized with 2.5, 5 and 7.5 wt% of TiO₂ with respect to g-C₃N₄. Same procedure was followed for TiO₂ synthesis without g-C₃N₄. It is known any variation in synthesis parameters, such as temperature, pH, reaction time, stirring rate, and autoclave cooling time can lead to the variation in the morphology and particle size. Thus, in order to have consistent results, we tried our best to keep all synthesis parameters constant, to get reproducible results.

2.3 Characterization

The crystallographic information of the photocatalysts was obtained by recording X-Ray diffraction (XRD) patterns using Bruker D8 advance X-Ray diffractometer with Cu K α X-rays within 2 θ range of 20–80 degree (0.5 degree per minute). Similarly, diffused reflectance spectra (DRS) of all samples were recorded in a JASCO UV–Vis–NIR spectrophotometer model V-670 within range of 300–650 nm (with interval of 2 nm). The morphology and composition of photocatalysts were confirmed using Field Emission Scanning Electron Microscopy (FESEM, JEOL, JSM-7610 F plus) and energy-dispersive spectroscopy (EDS) attached to FESEM. Photoluminescence (PL) spectra were recorded at room temperature using Fluorolog HORIBA JOBINYVON with excitation wavelength of 325 nm.

2.4 Measurement of photocatalytic activity

The photocatalytic activity of photocatalysts were evaluated by the degradation of RhB dye. 20 mg photocatalyst was used to degrade 20 ml aqueous solution of RhB having concentration 10⁻³ M. This solution was stirred in the dark for 45 min to achieve the adsorption–desorption equilibrium before light irradiation. After that, light from the xenon lamp having power 35 W (30,000 lx) was illuminated on the dye solution with the photocatalysts. The temperature of the dye solution was maintained at room temperature by keeping the beaker of the dye solution in the water bath. After each fixed time interval 2 ml solution was collected and centrifuged to exclude trace impurities or photocatalyst. Finally, the collected solutions were analysed by measuring absorbance with the help of UV–Vis spectrophotometer. The minimization in the RhB absorption peak intensity is the direct indication of the dye degradation.

2.5 ROS and pH studies

To identify reactive oxygen species (ROS), 0.5 M solution of the scavengers, namely IPA, DMSO, ascorbic acid, and methanol were prepared. Thereafter, separate four solutions were prepared by addition of 1 ml scavenger solution into 20 ml RhB dye solution. Before the photocatalytic experiment, the solution was kept for stirring at 850 rpm for

20 min. Afterwards, photocatalytic experiment was carried out by dispersing the photocatalyst.

To understand how dye degradation activity affects the pH of the dye solution, it is very important to study the relation between pH and point of zero charge (PZC). For pH study of dye solution, pH was varied from 3 to 11 and the same photodegradation experiment were repeated. Whereas, to identify PZC, the pH of the experimental solution was varied from acidic to basic condition (i.e. 2–10).

2.6 Photocurrent studies

The photocatalyst powder was grinded well. Then, the photocatalysts powder was cylindrically pelletized (1 cm diameter and 1 mm in thickness) using 5 tone/(inch)² pressure. These pellets were used for photocurrent experiment. Two Ag contacts ($\sim 1 \text{ mm}^2$) were made with separation $\sim 5 \text{ mm}$. The photocurrent measurements were performed by focusing simulated light of xenon lamp using illumination intensity of 200 mW/cm^2 (AM 1.5) using potentiostat (Metrohm Autolab PGSTAT302 N) under the variation of applied potential from 0.0 to 0.5 V.

3 Results and discussion

3.1 Structural studies

The XRD patterns were used to identify the crystal structure and phase of the photocatalysts. The XRD pattern (Fig. 1a) of $\text{g-C}_3\text{N}_4$ is resembling with JCPDS card no. 87-1526. Moreover, the preferential orientation along the (002) plane is the characteristic of layered structure of $\text{g-C}_3\text{N}_4$ [24, 26]. On the other hand, the XRD pattern of TiO_2 (Fig. 1b) showed polycrystalline nature with orientation along the planes (101), (004), (200), (105), (211), (204), and (116). All peak positions confirm the anatase phase of TiO_2 as it perfectly matches with JCPDS card no. 78-2486 [27].

The XRD patterns (Fig. 1c) of a series of $\text{TiO}_2/\text{g-C}_3\text{N}_4$ heterojunction photocatalysts with different wt% of TiO_2 (2.5TG, 5TG, and 7.5TG) are well crystalline in nature and showing the presence of both phases of $\text{g-C}_3\text{N}_4$ as well as TiO_2 . The intensity of XRD peaks corresponding to TiO_2 (denoted by *) was found to be increased with increase in wt% of TiO_2

concentration. The XRD results indicate that TiO_2 coverage is increased with increase in TiO_2 loading in the photocatalysts [28].

3.2 Morphological and compositional studies

Morphology of the nanostructures is one of the major feature which can decide the photocatalyst performance [29, 30]. The FESEM images of all photocatalysts are shown in Fig. 2. The higher magnification images of the respective photocatalysts are shown, wherein corresponding lower-magnification images are also shown as insets. The FESEM image as shown in Fig. 2a indicates the pristine $\text{g-C}_3\text{N}_4$ has the layered or sheet-like structure with hundreds of nm in sheet size as shown in the blue circle. Whereas, uniformly grown spherical nanoparticles of pristine TiO_2 are less than 100 nm in size. Moreover, at few places, agglomeration of individual TiO_2 nanoparticles was also observed as shown in Fig. 2b [31]. FESEM images (Fig. 2c–e) of 2.5TG, 5TG and 7.5TG heterojunction photocatalysts illustrate that in all the photocatalysts the TiO_2 particles are uniformly loaded onto $\text{g-C}_3\text{N}_4$ sheets. The blue circle drawn in FESEM images of 2.5TG, 5TG and 7.5TG heterojunction photocatalysts clearly indicates the sheet-like morphology of $\text{g-C}_3\text{N}_4$ loaded with spherical TiO_2 nanoparticles. Further with increase in wt% of TiO_2 loading on $\text{g-C}_3\text{N}_4$ sheets, more dense coverage of TiO_2 was detected and overall particle size was found to be increased. Figure 2f shows the elemental composition via EDS of 5TG composite and it clearly confirms the existence of Ti, C, N and O elements. Incidentally, EDS compositional analysis shows that nitrogen is the dominating element which means $\text{g-C}_3\text{N}_4$ acts as the base or host material [32].

3.3 Optical studies

The optical studies are mandatory for meticulous understanding of bandgap, absorption edges and heterojunction formation of the photocatalysts. The DRS of pristine TiO_2 and $\text{g-C}_3\text{N}_4$ and their heterojunction photocatalysts are shown in Fig. 3a. The absorption edges of pristine $\text{g-C}_3\text{N}_4$ and TiO_2 are located at ~ 455 and $\sim 405 \text{ nm}$, respectively. Further, it is observed that the absorption edges of the heterojunction photocatalysts lie in between the absorption edges of TiO_2 and $\text{g-C}_3\text{N}_4$ in the regime of

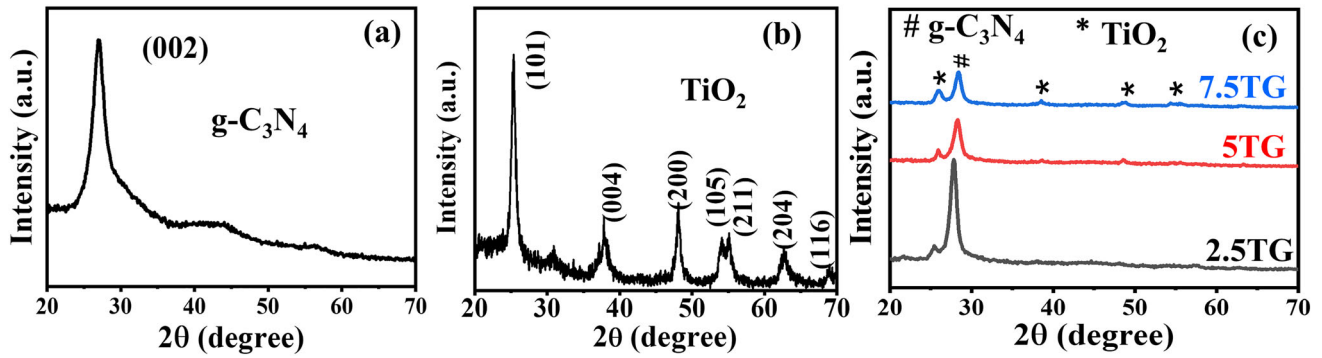


Fig. 1 XRD patterns of **a** g-C₃N₄, **b** TiO₂, **c** 2.5TG, 5TG and 7.5TG (# and * indicate XRD peaks corresponding to g-C₃N₄ and TiO₂) photocatalysts

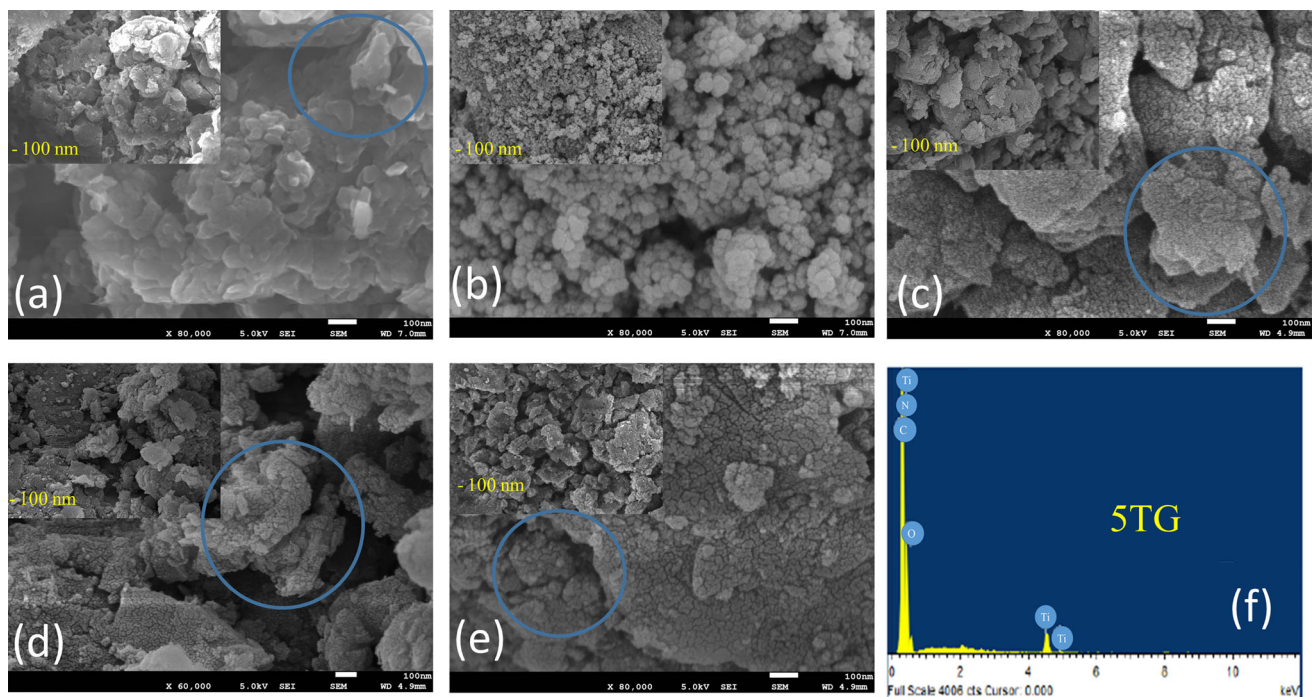


Fig. 2 FESEM images of **a** pristine g-C₃N₄, **b** pristine TiO₂, **c** 2.5TG, **d** 5TG and **e** 7.5TG photocatalyst. The inset of each FESEM image is lower-magnification FESEM image of that

photocatalyst. The scale bar represents 100 nm; **f** EDS of 5TG heterojunction photocatalyst

~ 440–448 nm. In comparison with pristine TiO₂, red shift occurs for all heterojunction photocatalysts indicating higher absorption of visible light, which may lead to higher visible radiation photocatalytic activity. In Fig. 3b, the bandgap values were estimated by Kubelka–Munk (KM) function $(F(r) \cdot hv)^2$ vs. photon energy ($h\nu$). To determine the bandgap of the material, i.e. plot of $(F(r) \cdot hv)^2$ vs. $h\nu$, the linear regime was extrapolated and x-axis intercept was considered as bandgap of the material [24]. Whilst the absorption edge of TiO₂ is observed at ~ 405 nm and its

bandgap found to be 3.06 eV, indicating it is responsive mostly under UV light exposure [33]. The bandgap of pristine g-C₃N₄ is 2.73 eV. However, variation in the loading amount can bring difference in the bandgap values. With increasing wt% of TiO₂ loading in the heterojunction photocatalysts, the bandgap energy increased from 2.77 to 2.87 eV (2.5TG:2.77 eV, 5TG:2.82 eV and 7.5TG:2.87 eV), i.e. in comparison with g-C₃N₄ photocatalyst blue shift occurs. The increment in the wt% of TiO₂ loading over g-C₃N₄ enhanced the bandgap and results in

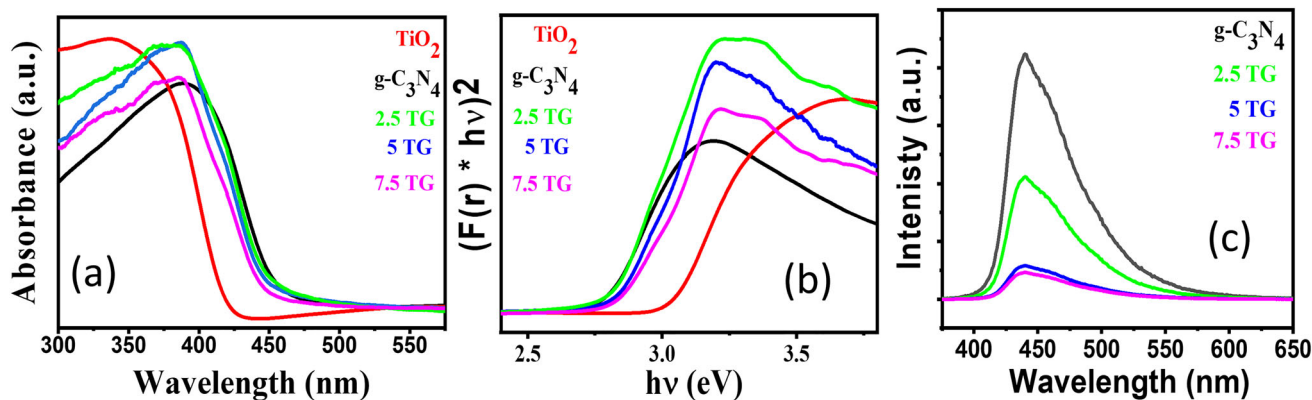


Fig. 3 a DRS, b Plots of $(F(r) \cdot hv)^2$ vs. photon energy and c PL spectra of $g\text{-C}_3\text{N}_4$, TiO_2 , 2.5TG, 5TG and 7.5TG photocatalysts

variation in heterojunction properties due to modification in electronic structure at the interface. The results of the DRS and KM plots are matching well suggesting more absorption of visible light, i.e. generation of photogenerated charge carriers for the heterojunction photocatalysts, under visible radiation.

PL is a versatile technique to monitor the rate of recombination and charge separation of photoinduced charge carriers. Figure 3c represents the PL spectra of $g\text{-C}_3\text{N}_4$ and all heterojunction photocatalysts. Amongst all, the PL intensity of the pristine $g\text{-C}_3\text{N}_4$ was found to be most intense signifying high rate of charge recombination. With increasing TiO_2 loading, the continuous decrement in peak intensity was resulted for all heterojunction photocatalysts. Previously, such a phenomenon was attributed to suppression of the recombination rate of electron-hole pairs and efficient charge transfer at the interface of heterojunction photocatalysts [22]. Moreover, such a scenario has been proved as necessary criterion to achieve excellent photocatalytic activity. In a nutshell, we successfully tailored the bandgap for suitable light absorption and reduced the charge recombination rate by modifying the interface of the heterojunction photocatalysts via appropriate charge transfer processes.

3.4 Photocatalytic degradation performance

To evaluate photocatalytic performance of prepared heterojunction photocatalysts, cationic dye RhB was used. The photocatalytic performance was tested at different time intervals under 35 W xenon lamp illumination using UV-Vis absorption spectroscopy.

The known quantity of the photocatalyst (20 mg) was added into the aqueous solution of the RhB dye (20 ml) and kept in the dark for the 45 min to adsorb the dye over the photocatalyst and then the said solution were kept under 35 W light source. We have performed experiment of RhB dye degradation for 5 min for all photocatalysts to determine superior photocatalyst amongst all as shown in Fig. 4a; the absorption spectra revealed that the peculiar absorption peak of RhB solution is at ~ 554 nm. It is well known that decrease in the absorption peak intensity of RhB dye occur because of decolourisation of the solution (i.e. dye degradation) due to photocatalytic activity. For all (2.5TG, 5TG and 7.5TG) photocatalyst different degrees of photodegradation was noted as shown in supplementary information Fig. S1a–c. To calculate the total time required for almost complete degradation, experiments were performed three times and average time was considered for data plotting. The corresponding graph is represented in supplementary information Fig. S1d.

The photodegradation performance was found to be improved in case of heterojunction photocatalysts than the pristine $g\text{-C}_3\text{N}_4$ and TiO_2 (Fig. 4a). Incidentally, 5TG demonstrated outstanding photocatalytic performance. Further studies were performed on the best-performing photocatalyst, i.e. 5TG. As shown in Fig. 4 (b), it is clearly observed that characteristics absorption peak of RhB dye gradually shifts towards 500 nm from 554 nm with increment in time-specifying dye degradation [28]. During this, the colour of RhB dye solution gradually transforms from dark pink to colourless. Additionally, the percentage photodegradation (% D) of RhB was calculated using following formula [12, 34].

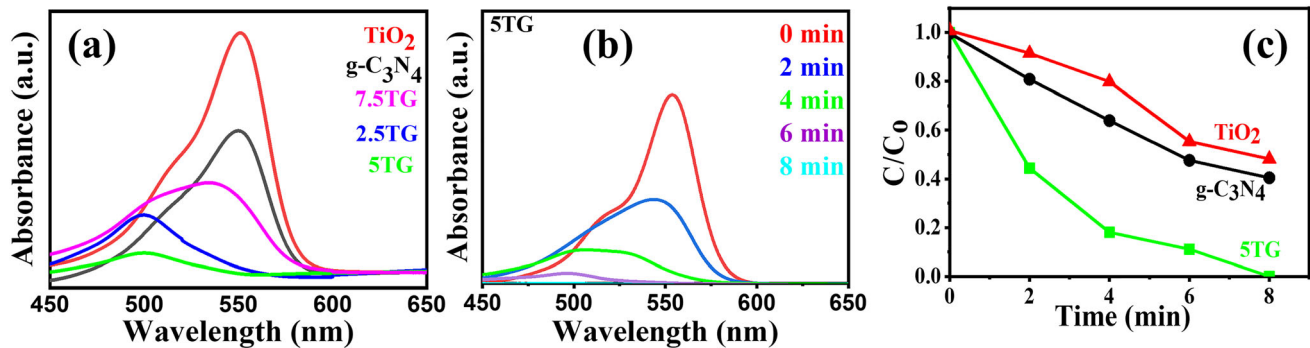


Fig. 4 **a** UV-Vis absorption spectra of RhB degradation using prepared different photocatalysts after 5 min, **b** UV-Vis absorption spectra of RhB degradation at different time intervals using 5TG photocatalyst, **c** Photodegradation [C/C_0 vs. time]

performance of RhB using g-C₃N₄, TiO₂ and 5TG photocatalysts after 8 min. All the photodegradation measurements were performed under 35 W xenon lamp irradiation

$$\% D = (C_0 - C) / C_0 \times 100 \quad (1)$$

where C_0 represents the concentrations of RhB after dark adsorption equilibrium and C represents the concentrations of RhB after irradiation time ' t '. The comparison of percentage photodegradation (% D) of RhB using g-C₃N₄, TiO₂ and 5TG after 4 and 8 min under light irradiation is presented in Fig S2(a), whereas exact % D of RhB using 5TG photocatalyst at interval of 2 min are represented in supplementary information Fig S2(b).

Figure 4c gives the evidence for photodegradation performance of 5TG composite to degrade RhB is much higher as compared to pristine TiO₂ and g-C₃N₄. The holistic study of the photocatalysis was performed by calculating the rate constant (k) of 5TG photocatalyst and compared with pristine TiO₂ and g-C₃N₄. The mathematical form of the pseudo-first-order kinetic model is given as [35]

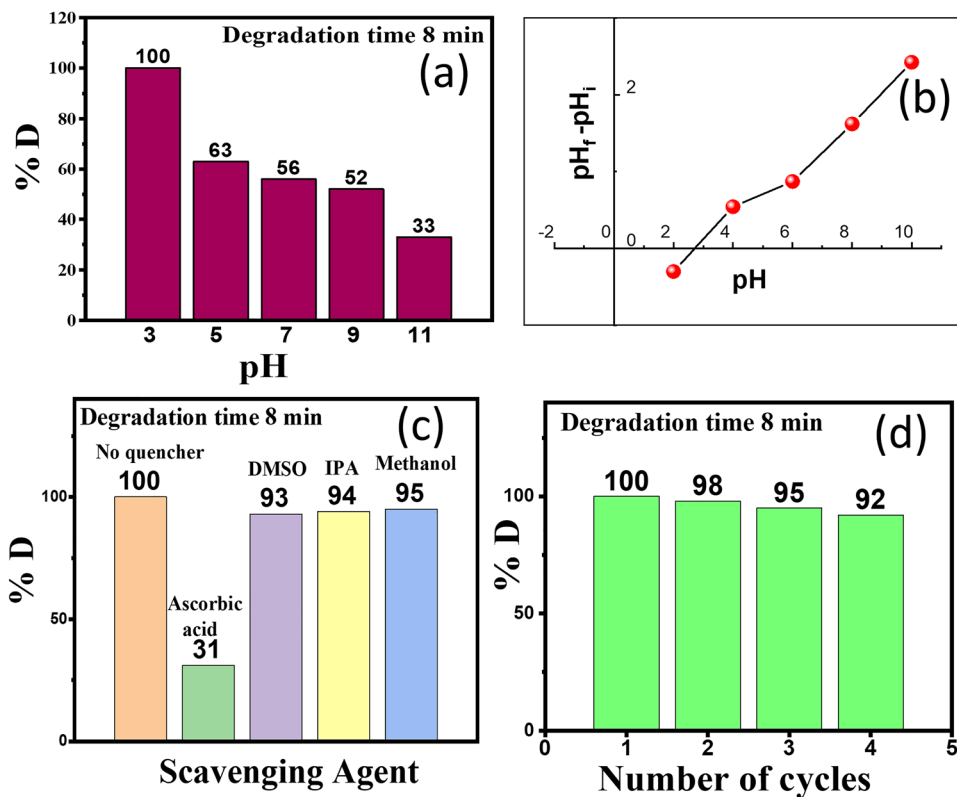
$$-\ln(C/C_0) = kt \quad (2)$$

The plot of $-\ln(C/C_0)$ verses time (Fig. S3) indicating that the overall kinetics of degradation of RhB accordingly with a first-order reaction. The degradation rate constants achieved for 5TG, g-C₃N₄ and TiO₂ photocatalyst were 0.75, 0.11 and 0.09 min⁻¹, respectively, as shown in supplementary information Fig. S3. The photocatalyst 5TG shows better performance than pristine g-C₃N₄ and TiO₂, as the rate constant of 5TG composite is almost 7 times greater than the rate constant of g-C₃N₄ and around 9 times greater than rate constant of TiO₂.

3.4.1 Effect of pH

It is well known that the pH of dye containing solution governs the electrostatic interaction between photocatalyst and dye molecules. Therefore, the dye degradation activity is significantly affected by the pH of dye containing solution. On the other hand, it is necessary to understand the relation between pH and point of zero charge (PZC). Whenever the pH is equal to PZC the surface of the photocatalyst becomes neutral. However, variation in the pH value (or its deviation from PZC) leads to interaction of the dye molecules on the photocatalyst and finally the photocatalyst achieves positive or negative charge [36]. Whenever adsorption of dye molecules occurs over photocatalyst due to electrostatic attraction between them the radicals are generated, which decides the overall degradation performance [12]. For the said study, the pH of dye solution (initial pH was around 4) was adjusted from 3 to 11 using 5 mM NaOH or HCl aqueous solutions. Figure 5a illustrates the effect of pH on the photodegradation of RhB dye solution using 5TG photocatalyst. The rate of photodegradation reaction was higher in acidic medium and photocatalytic performance remained constant for pH lower than 3. To divulge the reason behind this, we carried out one more experiment for identification of PZC value of the said photocatalyst. NaCl (40 ml, 0.01 M) aqueous solution was prepared in five beakers. The pH values of five solutions were adjusted to different values 2, 4, 6, 8 and 10 using 0.1 M NaOH or HCl aqueous solutions and considered as pH_i. Then in each beaker 0.1 g 5TG photocatalyst was added and the solution was kept for

Fig. 5 a Effect of pH on the photodegradation of RhB dye solution using 5TG photocatalyst, b PZC of 5TG photocatalyst, c ROS trapping study for the photodegradation of RhB dye solution using 5TG photocatalyst and d Cyclic stability test of photodegradation of RhB dye solution using 5TG photocatalyst



stirring for one day. Finally, the pH values were measured and denoted as pH_f . To calculate the PZC value, pH drift test (i.e. by plotting pH_i vs. $pH_f - pH_i$) was utilized. The corresponding plot is shown in Fig. 5b. The x-axis intercept is nothing but PZC and it was 2.7 for 5TG photocatalyst [37]. Whenever, the pH of the dye solution is greater than the PZC, it leads to negatively charged 5TG photocatalyst surface leading to the adsorption of the cationic RhB dye [38].

3.4.2 ROS trapping study

As explained above, adsorption of the dye over photocatalyst results into generation of ROS. To determine which ROS plays a vital role in degradation process of RhB dye, various radical trapping experiments were performed on 5TG photocatalyst. To trap and remove the radicals, these experiments were carried out using series of radical scavengers with addition of IPA, DMSO, ascorbic acid and methanol for quenching active species, such as hydroxyl radicals ($\bullet OH$), electrons (e^-), superoxide radicals ($\bullet O_2^-$) and holes (h^+), respectively [12, 39, 40]. The photodegradation activity of RhB is different for various scavengers; however, % D was

reduced for all scavengers as shown in Fig. 5c. The obtained photocatalytic performance was considered as 100% without use of any scavenger. In comparison to that, reduction in percentage degradation was found to be 94% (IPA), 93% (DMSO), 31% (ascorbic acid) and 95% (methanol). It is well known that ascorbic acid possesses high affinity to react with $\bullet O_2^-$ leading to suppress the $\bullet O_2^-$ radicals. Similarly, in case of 5TG photocatalyst, ascorbic acid demonstrated highest suppression of the $\bullet O_2^-$ radicals. As a result, we can conclude that $\bullet O_2^-$ radicals are the prominent reactive species, which play essential role in the decomposition of RhB. Whilst, other ROS such as electrons, $\bullet OH$ radicals and holes possess minor contribution in the degradation activity.

3.4.3 Recyclability of photocatalyst

Aiming to actual practical application of any photocatalyst, its cyclic stability and reusability are the most crucial parameters. Therefore, photocatalyst should be clearly dispersible in the dye solution during the degradation process and afterwards it should be separated from the solution easily. After the first use, the photocatalyst was washed with

DDW (four times) and ethanol (one time) and followed by its drying in air at 80 °C. Thereafter, reused for the further photocatalytic experiment. Similarly, the 5TG photocatalyst was used four times. Figure 5d shows the outstanding efficiency of 5TG photocatalyst for photodegradation of RhB dye up to four cycles. During repetitive use of the photocatalyst, minute loss (2–3%) in the activity was found. The major reason behind excellent photostability and reusability of 5TG photocatalyst is the homogeneous hybridization between g-C₃N₄ and TiO₂ [41]. Moreover, it can produce enough and appropriate number of ROS, which enhances the degradation rate. Slight decrease in the % D was observed due to loss of photocatalyst after each cycle in the recovery process [42]. Briefly it comes to the point, the said photocatalyst remain stable after 4 usable cycles and hence the said photocatalyst can be used in practical photodegradation.

3.4.4 Photocatalytic mechanism

To reveal reasons behind the outstanding photocatalytic performance, locations of the band edge positions, i.e. valence band (VB) and conduction band (CB) of each photocatalyst are demanded. Moreover, the relative position of CB and VB of photocatalyst can shed the light on the type of the heterojunction. Therefore, we have calculated the respective band edge positions of a semiconductor photocatalyst using the following empirical equation [43, 44]:

$$E_{VB} = \chi - E_e + 0.5E_g, \quad (3)$$

$$E_{CB} = E_{VB} - E_g, \quad (4)$$

where E_{VB} and E_{CB} are, respectively, for VB edge potential and CB edge potential. χ is the absolute electronegativity of the semiconductor. The values of χ for TiO₂ and g-C₃N₄ are 5.81 and 4.73 eV, respectively. E_e is the energy of free electrons on the hydrogen scale and it is 4.5 eV vs. NHE [45]. As mentioned above, the bandgap (E_g) values of TiO₂ and g-C₃N₄ were estimated and found to be 3.06 and 2.73 eV, respectively. Accordingly, using Eqs. 3 and 4, the values of E_{VB} of TiO₂ and g-C₃N₄ were calculated to be 2.84 and 1.59 eV vs. NHE, respectively, whereas E_{CB} values were -0.22 and -1.14 eV vs. NHE, respectively. By considering calculated values, the band structures of each photocatalyst is schematically illustrated in Fig. 6. It is essential to

note that the type II heterojunction formation takes place for the said photocatalysts.

Figure 6 shows schematic photodegradation mechanism involved in the present study. Upon light absorption, g-C₃N₄ generates e⁻ – h⁺ pairs. It is noteworthy that the CB potential of the g-C₃N₄ is relatively more negative than the CB potential of TiO₂. Thus, electrons move to CB of TiO₂ via closed interfacial regions between g-C₃N₄ and TiO₂, i.e. TiO₂ acts as sink for electrons. This heterojunction (type II) helps for separation of photoinduced charges. The reduction potential of O₂ is so placed that it is more positive than the CB potentials of g-C₃N₄ and TiO₂ leading to the transfer of the electrons to it. Furthermore, these electrons interact with O₂ (present in the solution) resulting into generation of [•]O₂⁻ radical species. On the other hand, since VB of the g-C₃N₄ is more negative than the standard redox potential E^0 (OH/OH⁻, 1.99 V) indicating less probability of the oxidation of OH⁻ or H₂O to form [•]OH due to photoinduced h⁺ in the VB of g-C₃N₄. In such a way, this active interface leads to separation of the photoinduced charges. Finally, reaction of RhB/RhB⁺ with [•]O₂⁻ radical species and h⁺ occur and degradation of the dye takes place [46–48].

To support the above statements, the enhanced photocatalytic activity of 5 wt% TiO₂ loaded /g-C₃N₄ heterojunction, charge transfer was studied by photocurrent measurement. Fig. S4 represents the I–V characteristics of all TiO₂/g-C₃N₄ heterojunctions. Under light illumination, as compared to 7.5TG and 2.5TG, the maximum photocurrent was observed for

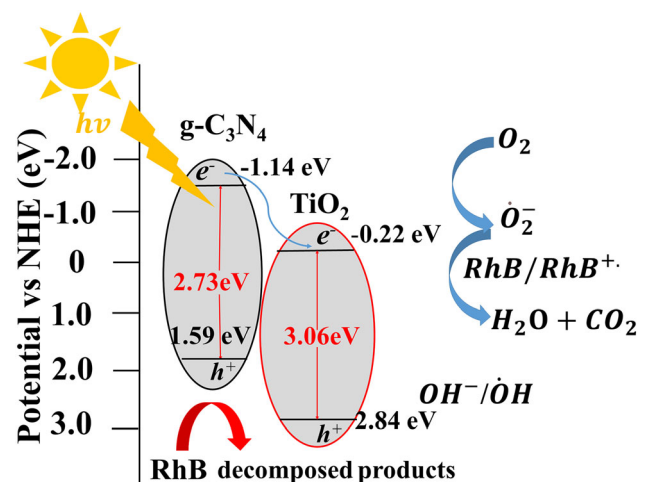


Fig. 6 Schematic representation of RhB photodegradation mechanism due to 5TG photocatalyst

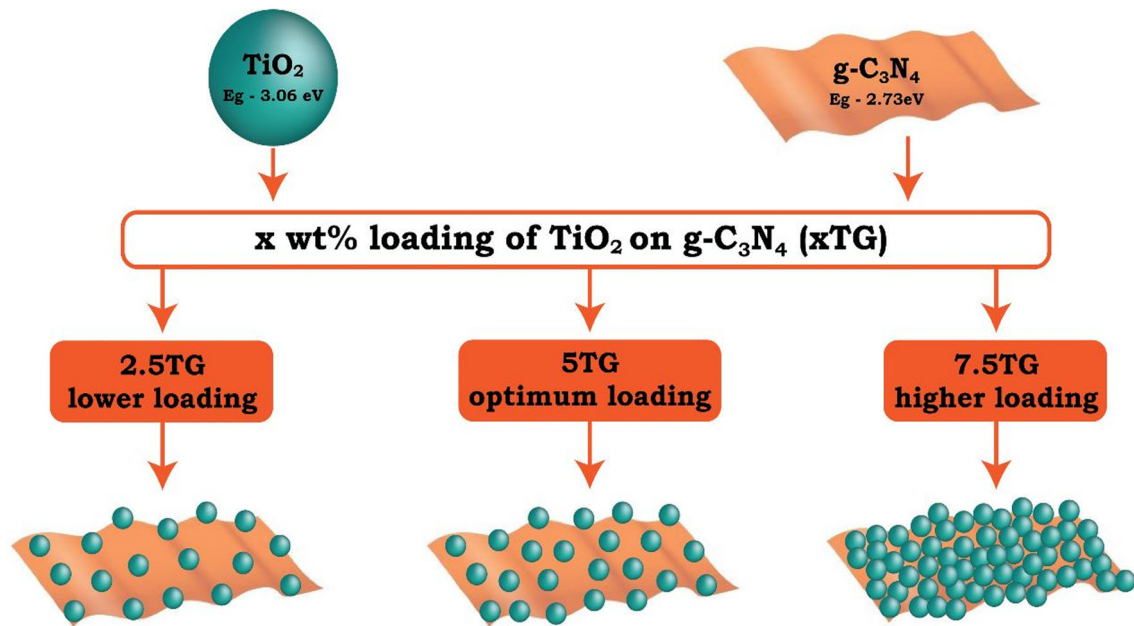


Fig. 7 Schematic diagram of loading of TiO_2 on $\text{g-C}_3\text{N}_4$ sheets in $x\text{TG}$ ($x = 2.5, 5, 7.5$ wt%) heterojunction photocatalysts

5TG. The increment in the photocurrent shows the formation of active heterojunction due to transfer of photocharges. In other words, due to light absorption, $e^- - h^+$ pairs are originated and cross-over across junctions.

We observed that the photocatalytic performance of $\text{g-C}_3\text{N}_4$ and TiO_2 is underrated as compared to another heterojunction photocatalysts. However, it is intriguing to understand the rationale behind variation in the photocatalytic performance of the (2.5TG, 5TG and 7.5TG) heterojunction photocatalysts. The overall photocatalytic performance is the synergetic effect of several features, such as bandgap, interfacial contact between photocatalysts, photoinduced charge generation, recombination rate, type of heterojunction, and visible light absorption.

Let us try to understand the effect of above-said features on photocatalytic performance of heterojunction photocatalysts, i.e. 2.5TG, 5TG and 7.5TG. The loading of TiO_2 over $\text{g-C}_3\text{N}_4$ plays a vital role and possesses prime importance to decide the final photocatalytic performance due to alteration in interfacial region. The sheet-like structures of $\text{g-C}_3\text{N}_4$ are higher in dimension as compared to TiO_2 particles as observed in the FESEM images. Besides that, loading of TiO_2 over $\text{g-C}_3\text{N}_4$ form nanojunctions through their interfacial regions. We have varied three different wt% loadings of TiO_2 onto $\text{g-C}_3\text{N}_4$ and for simplistic analysis we name them as lower

(2.5TG), optimum (5TG) and higher (7.5TG) loadings as depicted in Fig. 7.

For lower loading, the interfacial region is very less, since the $\text{g-C}_3\text{N}_4$ is sparsely covered with TiO_2 . Additionally, with optimum loading, the $\text{g-C}_3\text{N}_4$ is almost covered with TiO_2 leading to the perfect interfacial region, whereas for higher loading surface of $\text{g-C}_3\text{N}_4$ is abundantly covered by TiO_2 . The above-said statements are supported by the optical absorption studies since bandgap is found to be shifted to higher values with increment in the wt% loading of TiO_2 . The bandgaps of all heterojunction photocatalyst remains in the region of 2.77 to 2.87 eV; they respond very well under visible light radiation in production of sufficient number of $e^- - h^+$ pairs [49, 50]. Lower loading provides inadequate nanojunctions between $\text{g-C}_3\text{N}_4$ and TiO_2 and lesser bandgap. Moreover, optimum loading gives rise to the favourable nanojunctions or perfect interfacial regions so that charge generation and its transfer is superior. Whereas, at higher loading, the overgrowth of TiO_2 is possible which blocks the light interaction with $\text{g-C}_3\text{N}_4$, i.e. TiO_2 acts like barrier. Additionally, as observed in PL spectra, the interfacial region of the optimum loaded photocatalysts can demonstrate its usefulness to charge separation, i.e. increases the life time of separated electrons and holes. By contrast, for lower and higher loading, greater charge separation was observed due to disproportionate amount of

Table 1 Comparison of degradation rate constant, time and degree measured under different light source intensities, radicals involved with respect to degradation of RhB dye and best-performing photocatalysts prepared from g-C₃N₄ and TiO₂ using different methods

Sr. No.	Preparation method	Light source	Degradation rate constant	Degradation time and degree of degradation	Radicals	References
1	Solvothermal method	Solar radiation	0.04973 min ⁻¹	–	–	[51]
2	Hard template method	500 W	0.0335 min ⁻¹	100 min, 96.5%	–	[52]
3	Co-precipitation method	100 W	0.17 min ⁻¹	–	Holes and •OH	[26]
4	Biomimetic approach under relative mild condition	500 W Xe lamp	0.261 h ⁻¹	5 h, 84%	•O ₂ ⁻	[28]
5	Co-precipitation method	500 W	–	20 min, 99%	Holes and •OH	[26]
6	Hydrothermal method	350 W Xe arc lamp	–	80 min, 95.2%	•O ₂ ⁻ and holes	[53]
7	Ball milling and microwave	300 W Xe lamp	0.0841 min ⁻¹	30 min, 89.44%	•O ₂ ⁻	[23]
8	Calcination method	350 W Xe arc lamp	0.0478 min ⁻¹	80 min.	•O ₂ ⁻ and holes	[47]
9	Solvothermal method	70,000 and 80,000 lx	–	50 min, 100%	–	[51]
10	Molten salt method	300 W Xe lamp	0.047 min ⁻¹	60 min, 95%	–	[54]
11	Sol-gel and Spin-coating method	300 W Xe lamp	0.00218 min ⁻¹	180 min.	•O ₂ ⁻ and •OH	[55]
12	Hydrothermal method	30 W cold visible light emitting diode	0.0356 min ⁻¹	–	•O ₂ ⁻	[56]
13	Dispersion method	300 W Xe lamp	0.00448 min ⁻¹	300 min, 76%	•O ₂ ⁻ and •OH	[57]
14	Microwave hydrothermal treatment	10 W LED lamp	0.0949 min ⁻¹	40 min, 97.6%	•OH	[33]
15	Hydrothermal treatment	300 W Xe lamp	0.189 min ⁻¹	–	•O ₂ ⁻	[58]
16	Hydrothermal method	35 W Xe lamp (30,000 lx)	0.75 min ⁻¹	8 min, 100%	•O ₂ ⁻	This work

g-C₃N₄ and TiO₂. In brief, the photocatalytic enhancement in optimum (5TG) heterojunction photocatalyst is attributed to generation of desirable photoinduced charges and improved charge separation via type II heterojunction, reactive active species especially •O₂⁻ radicals, etc.

Variation in light source intensity and wavelength, concentration of dye solution and quantity of photocatalyst is found in previous reports on g-C₃N₄ and TiO₂ composites/heterojunction photocatalysts. Thus, comparison of the photocatalytic performance on the same platform is a challenge. However, to get rough idea, we have compared the photocatalytic performance achieved in this work with literature in Table 1. The degradation rate constant/efficiency values achieved in our work are superior to the most of previous proclaimed values.

4 Conclusion

In summary, a series of TiO₂/g-C₃N₄ heterojunction photocatalyst are successfully synthesized via hydrothermal method. The prepared type II heterojunction photocatalyst showed excellent photodegradation performance towards RhB dye under 35 W xenon light with the good stability. Moreover, the highest degradation rate was achieved for 5 wt% loading of TiO₂ on g-C₃N₄ as 0.75 min⁻¹ and complete degradation was occurred within 8 minutes. Quantitatively speaking, the degradation rate of above heterojunction photocatalyst is ~ 7 times and ~ 9 times greater than that of degradation rate of pristine g-C₃N₄ and TiO₂, respectively. The point of zero charge (PZC) of the heterojunction photocatalyst is 2.7 and we observed highest degradation rate in acidic

medium (pH = 3). It is observed that superoxide radicals ($\cdot\text{O}_2^-$) are the prominent reactive species for the decomposition of RhB dye. Better light absorption, improved charge separation and transfer occurred via active interfacial regions between TiO_2 and g- C_3N_4 sheets leading to the outstanding photocatalytic performance than previous reports. 5 wt% loaded $\text{TiO}_2/\text{g-C}_3\text{N}_4$ photocatalyst exhibited recyclability with high activity (92% after 4 cycles) and thus, we believe that its potential in industrial water treatment can bring solutions to sustainable environment.

Acknowledgements

The authors are thankful to Prof. Dr. Parasharam M. Shirage, Indian Institute of Technology (IIT) Indore, Indore, India for providing FESEM instrumental facility. Authors are also thankful to Prof. Dr. S. R. Jadhkar and Ms Shruti Shah, Department of Physics, Savitribai Phule Pune University, Pune, India for their support in photocurrent measurements.

Author contribution

SMY contributed to conceptualization, data collection and analysis and manuscript writing, MAD contributed to data analysis, manuscript writing and editing, SDS contributed to supervision, review, editing and funding. All authors read and approved the final manuscript.

Funding

The authors are grateful to Savitribai Phule Pune University, Pune, India for the financial support.

Data availability

The authors confirm that the data supporting the findings of this study are available within the article and/or its supplementary materials.

Declarations

Competing interests The authors declare that they have no conflicts of interest.

Supplementary Information: The online version contains supplementary material available at <http://doi.org/10.1007/s10854-023-11019-z>.

References

1. J.-R.L. Chong-Chen, X.-L. Wang, Y.-Q. Lv, Zhang and Guangsheng Guo, photocatalytic organic pollutants degradation in metal-organic frameworks. *Energy Environ. Sci.* **7**, 2831–2867 (2014)
2. W. Liu, S. Chang, D. Liu, F. Wen, Three-dimensional ordered macroporous materials with g- C_3N_4 and TiO_2 as pore walls for efficient photocatalytic hydrogen evolution. *Colloids Surf. A* **609**, 125681 (2021)
3. A. Alaghmandfard, K. Ghandi, A comprehensive review of graphitic carbon nitride (g- C_3N_4)-metal oxide-based nanocomposites potential for photocatalysis and sensing. *Nanomaterials* **12**, 294 (2022)
4. J.A. Khan, M. Sayed, S. Khan, N.S. Shah, D.D. Dionysiou, G. Boczkaj, Advanced oxidation processes for the treatment of contaminants of emerging concern, in *Contaminants of Emerging Concern in Water and Wastewater* (Butterworth-Heinemann, Oxford, 2020), pp. 299–365
5. I. Chakraborty, Z. Guo, B. Anirban, P. Sahoo, Physical modifications and algorithmic predictions behind further advancing 2D Water Splitting Photocatalyst: an overview. *Eng. Sci.* **20**, 34–46 (2022)
6. M.M. Khan, S.F. Adil, A. Al-Mayouf, Metal oxides as photocatalysts. *J. Saudi Chem. Soc.* **19**, 462–464 (2015)
7. Z. Cheng, W. Qi, C.H. Pang, T. Thomas, T. Wu, S. Liu, M. Yang, Recent advances in transition metal nitride-based materials for photocatalytic applications. *Adv. Funct. Mater.* **31**, 2100553 (2021)
8. S. Wu, Z. Wu, X.L. Wang, X. Wang, R. Zhou, D.S. Li, T. Wu, Two new layered metal chalcogenide frameworks as photocatalysts for highly efficient and selective dye degradation. *Dalton Trans.* **49**, 13276–13281 (2020)
9. F. Lu, D. Astruc, Nanocatalysts and other nanomaterials for water remediation from organic pollutants. *Coord. Chem. Rev.* **408**, 213180 (2020)
10. J. Theerthagiri, S.J. Lee, K. Karuppasamy, S. Arulmani, S. Veeralakshmi, M. Ashokkumar, M.Y. Choi, Application of advanced materials in sonophotocatalytic processes for the remediation of environmental pollutants. *J. Hazard. Mater.* **412**, 125245 (2021)
11. Z. Sun, C. Li, G. Yao, S. Zheng, In situ generated g- $\text{C}_3\text{N}_4/\text{TiO}_2$ hybrid over diatomite supports for enhanced photodegradation of dye pollutants. *Mater. Design.* **94**, 403–409 (2016)

12. D. Monga, S. Basu, Enhanced photocatalytic degradation of industrial dye by g-C₃N₄/TiO₂ nanocomposite: role of shape of TiO₂. *Adv. Powder Technol.* **30**, 1089–1098 (2019)
13. S.B. Kokane, S.D. Sartale, K.G. Girija, R. Jagannath, Sasikala, Photocatalytic performance of pd decorated TiO₂-CdO composite: role of in situ formed CdS in the photocatalytic activity. *Int. J. Hydrog. Energy* **40**, 13431–13442 (2015)
14. J. Low, J. Yu, M. Jaroniec, S. Wageh, A.A. Al-Ghamdi, Heterojunction photocatalysts. *Adv. Mater.* **29**, 1601694 (2017)
15. H. Xu, J. Ju, W. Li, J. Zhang, J. Wang, B. Cao, Superior triethylamine-sensing properties based on TiO₂/SnO₂ n-n heterojunction nanosheets directly grown on ceramic tubes. *Sens. Actuators B* **228**, 634–642 (2016)
16. M. Humayun, F. Raziq, A. Khan, W. Luo, Modification strategies of TiO₂ for potential applications in photocatalysis: a critical review. *Green Chem. Lett. Rev.* **11**, 86–102 (2018)
17. K. Qi, B. Cheng, J. Yu, W. Ho, A review on TiO₂ -based Z-scheme photocatalysts. *Chin. J. Catal.* **38**, 1936–1955 (2017)
18. W. Al Zoubi, A.A. Salih Al-Hamdani, B. Sunghun, Y.G. Ko, A review on TiO₂-based composites for superior photocatalytic activity. *Rev. Inorg. Chem.* **41**, 213–222 (2021)
19. Y.J. Ren, D.Q. Zeng, W.J. Ong, Interfacial engineering of graphitic carbon nitride (g-C₃N₄)-based metal sulfide heterojunction photocatalysts for energy conversion: a review. *Chin. J. Catal.* **40**, 289–319 (2019)
20. M. Ismael, A review on graphitic carbon nitride (g-C₃N₄) based nanocomposites: synthesis, categories, and their application in photocatalysis. *J. Alloys Compd.* **846**, 156446 (2020)
21. H. Yan, H. Yang, TiO₂-g-C₃N₄ composite materials for photocatalytic H₂ evolution under visible light irradiation. *J. Alloys Compd.* **509**, L26–L29 (2011)
22. S. Zhao, S. Chen, H. Yu, X. Quan, g-C₃N₄/TiO₂ hybrid photocatalyst with wide absorption wavelength range and effective photogenerated charge separation. *Sep. Purif. Technol.* **99**, 50–54 (2012)
23. Y. Wang, J. Yu, W. Peng, J. Tian, C. Yang, Novel multilayer TiO₂ heterojunction decorated by low g-C₃N₄ content and its enhanced photocatalytic activity under UV, visible and solar light irradiation. *Sci. Rep.* **9**, 5932 (2019)
24. S.B. Kokane, R. Sasikala, D.M. Phase, S.D. Sartale, In₂S₃ nanoparticles dispersed on g-C₃N₄ nanosheets: role of heterojunctions in photoinduced charge transfer and photoelectrochemical and photocatalytic performance. *J. Mater. Sci.* **52**, 7077–7090 (2017)
25. S.B. Kokane, S.D. Sartale, C.A. Betty, R. Sasikala, Pd-TiO₂-SrIn₂O₄ heterojunction photocatalyst: enhanced photocatalytic activity for hydrogen generation and degradation of methylene blue. *RSC Adv.* **4**, 55539–55547 (2014)
26. M. Sharma, S. Vaidya, A.K. Ganguli, Enhanced photocatalytic activity of g-C₃N₄-TiO₂ nanocomposites for degradation of rhodamine B dye. *J. Photochem. Photobiol. A* **335**, 287–293 (2017)
27. S. Mugundan, P. Praveen, S. Sridhar, S. Prabu, K. Lawrence Mary, M. Ubaidullah, S.F. Shaikh, S. Kanagesan, Sol-gel synthesized barium doped TiO₂ nanoparticles for solar photocatalytic application. *Inorg. Chem. Commun.* **139**, 109340 (2022)
28. Z. Tong, D. Yang, T. Xiao, Y. Tian, Z. Jiang, Biomimetic fabrication of g-C₃N₄/TiO₂ nanosheets with enhanced photocatalytic activity toward organic pollutant degradation. *Chem. Eng. J.* **260**, 117–125 (2015)
29. M.A. Desai, A. Kulkarni, G. Gund, S.D. Sartale, SILAR grown K⁺ and Na⁺ ions preinserted MnO₂ nanostructures for supercapacitor applications: a comparative study. *Energy Fuels* **35**, 4577–4586 (2021)
30. M.A. Desai, S.D. Sartale, Facile soft solution route to engineer hierarchical morphologies of ZnO nanostructures. *Cryst. Growth. Des.* **15**, 4813–4820 (2015)
31. P. Gündoğmuş, J. Park, A. Öztürk, Preparation and photocatalytic activity of g-C₃N₄/TiO₂ heterojunctions under solar light illumination. *Ceram. Int.* **46**, 21431–21438 (2020)
32. S. Das, H. Mahalingam, Dye degradation studies using immobilized pristine and waste polystyrene-TiO₂/rGO/g-C₃N₄ nanocomposite photocatalytic film in a novel airlift reactor under solar light. *J. Environ. Chem. Eng.* **7**, 103289 (2019)
33. Y. Xia, L. Xu, J. Peng, J. Han, S. Guo, L. Zhang, Z. Han, S. Komarneni, TiO₂@g-C₃N₄ core/shell spheres with uniform mesoporous structures for high performance visible-light photocatalytic application. *Ceram. Int.* **45**, 18844–18851 (2019)
34. M.A. Hanif, J. Akter, Y.S. Kim, H.G. Kim, J.R. Hahn, L.K. Kwac, Highly efficient and sustainable ZnO/CuO/g-C₃N₄ photocatalyst for wastewater treatment under visible light through heterojunction development. *Catalysts* **12**, 151 (2022)
35. B. Ren, T. Wang, G. Qu, F. Deng, D. Liang, W. Yang, M. Liu, In situ synthesis of g-C₃N₄/TiO₂ heterojunction nanocomposites as a highly active photocatalyst for the degradation of Orange II under visible light irradiation. *Environ. Sci. Pollut. Res.* **25**, 19122–19133 (2018)
36. G. Cao, *Nanostructures & nanomaterials: synthesis, properties & applications* (Imperial College Press, Covent Garden, 2004)
37. N. Van Hung, B.T.M. Nguyet, N.H. Nghi, D.Q. Khieu, Photocatalytic degradation of Methylene Blue by using ZnO/

- Longan seed activated carbon under visible-light region. *J. Inorg. Organomet. Polym. Mater.* **31**, 446–459 (2021)
38. Y.-H. Chiu, T.-F. Chang, C.-Y. Chen, M. Sone, Y.-J. Hsu, Mechanistic insights into photodegradation of organic dyes using heterostructure photocatalysts. *Catalysts* **9**, 430 (2019)
 39. A. Mishra, A. Mehta, S. Kainth, S. Basu, Effect of g-C₃N₄ loading on TiO₂/Bentonite nanocomposites for efficient heterogeneous photocatalytic degradation of industrial dye under visible light. *J. Alloys Compd.* **764**, 406–415 (2018)
 40. A.R. Kuldeep, R.S. Dhabbe, K.M. Garadkar, Development of g-C₃N₄-TiO₂ visible active hybrid photocatalyst for the photodegradation of methyl orange. *Res. Chem. Intermed.* **47**, 5155–5174 (2021)
 41. M.A. Qamar, S. Shahid, M. Javed, S. Iqbal, M. Sher, M.B. Akbar, Highly efficient g-C₃N₄/Cr-ZnO nanocomposites with superior photocatalytic and antibacterial activity. *J. Photochem. Photobiol. A* **401**, 112776 (2020)
 42. D. Chaudhary, V.D. Vankar, N. Khare, Noble metal-free g-C₃N₄/TiO₂/CNT ternary nanocomposite with enhanced photocatalytic performance under visible-light irradiation via multi-step charge transfer process. *Sol. Energy* **158**, 132–139 (2017)
 43. I. Troppová, M. Šihor, M. Reli, M. Ritz, P. Praus, K. Kočí, Unconventionally prepared TiO₂/g-C₃N₄ photocatalysts for photocatalytic decomposition of nitrous oxide. *Appl. Surf. Sci.* **430**, 335–347 (2018)
 44. M.A. Desai, V. Sharma, M. Prasad, G. Gund, S. Jadkar, S.D. Sartale, Photoelectrochemical performance of MWCNT–Ag–ZnO ternary hybrid: a study of ag loading and MWCNT garnishing. *J. Mater. Sci.* **56**, 8627–8642 (2021)
 45. G.W. Ruirui Hao, C. Jiang, H. Tang, Q. Xu, In situ hydrothermal synthesis of g-C₃N₄/TiO₂ heterojunction photocatalysts with high specific surface area for rhodamine B degradation. *Appl. Surface Sci.* **411**, 400–410 (2017)
 46. L.C. Sim, K.S. Koh, K.H. Leong, Y.H. Chin, A.A. Aziz, P. Saravanan, In situ growth of g-C₃N₄ on TiO₂ nanotube arrays: construction of heterostructures for improved photocatalysis properties. *J. Environ. Chem. Eng.* **8**, 103611 (2020)
 47. R. Hao, G. Wang, H. Tang, L. Sun, C. Xu, D. Han, Template-free preparation of macro/mesoporous g-C₃N₄/TiO₂ heterojunction photocatalysts with enhanced visible light photocatalytic activity. *Appl. Catal. B* **187**, 47–58 (2016)
 48. R. Bibi, Q. Shen, L. Wei, D. Hao, N. Li, J. Zhou, Hybrid BiOBr/Uio-66-NH₂ composite with enhanced visible-light driven photocatalytic activity toward RhB dye degradation. *RSC Adv.* **8**, 2048–2058 (2018)
 49. M.A. Desai, A.N. Vyas, G.D. Saratale, S.D. Sartale, Zinc oxide superstructures: recent synthesis approaches and application for hydrogen production via photoelectrochemical water splitting. *Int. J. Hydrog. Energy* **44**, 2091–2127 (2019)
 50. M.A. Desai, V. Sharma, M. Prasad, S. Jadkar, G.D. Saratale, S.D. Sartale, Seed-layer-free deposition of well-oriented ZnO nanorods thin films by SILAR and their photoelectrochemical studies. *Int. J. Hydrog. Energy* **45**, 5783–5792 (2020)
 51. R.T. Thomas, N. Sandhyarani, Template free synthesis of graphitic carbon nitride/titania mesoflowers. *RSC Adv.* **5**, 72683–72690 (2015)
 52. S. Ma, J. Xue, Y. Zhou, Z. Zhang, Z. Cai, D. Zhu, S. Liang, Facile fabrication of a mpg-C₃N₄/TiO₂ heterojunction photocatalyst with enhanced visible light photoactivity toward organic pollutant degradation. *RSC Adv.* **5**, 64976–64982 (2015)
 53. R. Hao, G. Wang, C. Jiang, H. Tang, Q. Xu, In situ hydrothermal synthesis of g-C₃N₄/TiO₂ heterojunction photocatalysts with high specific surface area for rhodamine B degradation. *Appl. Surf. Sci.* **411**, 400–410 (2017)
 54. X. Yan, Q. Gao, J. Qin, X. Hui, Z. Ye, J. Li, Z. Ma, A facile method for fabricating TiO₂/g-C₃N₄ hollow nanotube heterojunction and its visible light photocatalytic performance. *Mater. Lett.* **217**, 1–4 (2018)
 55. W. Zhao, X. Yang, C. Liu, X. Qian, Y. Wen, Q. Yang, T. Sun, W. Chang, X. Liu, Z. Chen, Facile construction of all-solid-state Z-scheme g-C₃N₄/TiO₂ thin film for the efficient visible-light degradation of organic pollutant. *Nanomaterials* **10**, 600 (2020)
 56. K. Li, Z. Huang, X. Zeng, B. Huang, S. Gao, J. Lu, Synergetic effect of Ti³⁺ and oxygen doping on enhancing photoelectrochemical and photocatalytic properties of TiO₂/g-C₃N₄ heterojunctions. *ACS Appl. Mater. Interfaces* **9**, 11577–11586 (2017)
 57. D. Zhou, Z. Chen, Q. Yang, C. Shen, G. Tang, S. Zhao, J. Zhang, D. Chen, Q. Wei, X. Dong, Facile construction of g-C₃N₄ nanosheets/TiO₂ nanotube arrays as Z-scheme photocatalyst with enhanced visible-light performance. *Chem-CatChem* **8**, 1–11 (2016)
 58. W. Gu, F. Lu, C. Wang, S. Kuga, L. Wu, Y. Huang, M. Wu, Face-to-face interfacial assembly of ultrathin g-C₃N₄ and anatase TiO₂ nanosheets for enhanced solar photocatalytic activity. *ACS Appl. Mater. Interfaces* **9**, 28674–28684 (2017)

Publisher's Note Springer Nature remains neutral with regard to jurisdictional claims in published maps and institutional affiliations.

Springer Nature or its licensor (e.g. a society or other partner) holds exclusive rights to this article under a publishing agreement with the author(s) or other rightsholder(s); author self-archiving of the accepted manuscript version of this article is solely governed by the terms of such publishing agreement and applicable law.